Research Article | Vol. 29, No. 22 / 25 Oct 2021 / Optics Express 35580

Uncertainties in the reconstruction of nanostructures in EUV scatterometry and grazing incidence small-angle X-ray scattering

ANALÍA FERNÁNDEZ HERRERO,[1,*] MIKA PFLÜGER,[1,2] JANA PULS,[1] FRANK SCHOLZE,[1] AND VICTOR SOLTWISCH[1]

[1] *Physikalisch-Technische Bundesanstalt, Abbestr. 2-12, 10587 Berlin, Germany*
[2] *Potsdam Institute for Climate Impact Research (PIK) e. V., Telegrafenberg A 31, 14473 Potsdam, Germany*
[*] *analia.fernandez_herrero@helmholtz-berlin.de*

Abstract: Increasing miniaturization and complexity of nanostructures require innovative metrology solutions with high throughput that can assess complex 3D structures in a non-destructive manner. EUV scatterometry is investigated for the characterization of nanostructured surfaces and compared to grazing-incidence small-angle X-ray scattering (GISAXS). The reconstruction is based on a rigorous simulation using a Maxwell solver based on finite-elements and is statistically validated with a Markov-Chain-Monte-Carlo sampling method. It is shown that in comparison to GISAXS, EUV allows to probe smaller areas and to reduce the computation times obtaining comparable uncertainties.

© 2021 Optical Society of America under the terms of the OSA Open Access Publishing Agreement

1. Introduction

Measurement and characterization of nanofeatures correspond to more than 50% of the manufacturing process of the integrated electronic circuits [1]. Metrology methods must be able to resolve the structural complexity of the new nanostructures and provide accurate and efficient information. In-line metrology methods that are commonly used are critical dimension scanning electron microscopy (cd-SEM), critical dimension atomic force microscopy (cd-AFM) and optical scattering techniques, such as optical critical dimension (OCD) [1,2]. Scanning methods are well-established, and allow the direct investigation of the nanostructures but cannot be applied for characterizing more complex 3D structures. SEM cross-section analysis might involve the destruction of the target or a complex data analysis from top view images [3,4]. Atomic force microscopy (AFM) is limited by the accessibility of the tip. The manufacturing and characterization of the tip is posing itself a challenge due to the small dimensions [5]. And this data is also subjected to the deconvolution of the signal with the tip shape [6]. As an alternative to those methods, photon scattering does not destruct the sample and delivers ensemble average information. Optical scatterometry has been already implemented as in-line metrology for the control of each step in multiple patterning lithographic processes [7]. However, when shrinking the dimensions, the attainable resolution is not sufficient [8]. Small angle X-ray scattering (SAXS) uses wavelengths shorter than the structure sizes and can be used for probing the inhomogeneities in the electron density within a sample system. In this geometry, the samples are illuminated with the beam normal to the sample surface. By rotating this angle, periodic nanostructures can also be analyzed [9,10]. This method is known as CD-SAXS (critical dimension SAXS) and involves the acquisition of several images for different rotation angles. Depending on the sample, it is rotated up to 20∘ or 45∘ around the normal illumination [9,11]. However, the investigation of nanostructured surfaces can profit from grazing-incidence illumination. Grazing-incidence small angle X-ray scattering (GISAXS) has larger sensitivity to the surface. The advantages of GISAXS are ensemble results in short measurement times also on thick and non-homogeneous substrates in a non-destructive and contact free manner.

#430416 https://doi.org/10.1364/OE.430416
Journal © 2021 Received 5 May 2021; revised 25 Jun 2021; accepted 1 Jul 2021; published 15 Oct 2021

GISAXS has already been used for probing periodic nanostructures [12–21]. The reconstruction of lamellar gratings using GISAXS has been achieved with sub-nanometer resolution [18,20,22]. And the suitability for using GISAXS for the characterization of the impact of line-edge roughness on the scattering pattern has been reported [17,20]. However, the main disadvantage of GISAXS in comparison to previous scattering methods is the large footprint of the beam projected onto the sample. The dimension of the illuminated area usually exceeds any investigated target [19], which leads to contributions of scattered intensity from surrounding structures. Moreover, it has been shown that the beam divergence is a key parameter in the unequivocal reconstruction of nanostructures from GISAXS data [18,20]. But including the divergence of the beam in the reconstruction process increases the computation time [20]. EUV scattering allows the investigation of samples with steeper angles, reducing the footprint of the beam on the sample while keeping the surface sensitivity of the technique. Moreover, EUV delivers a better optical contrast for relevant materials in the semiconductor industry, including oxide layers. For instance, at-wavelength investigations of MoSi multilayer mirrors [23] can be carried out. Another known issue is the carbon contamination of the masks [24,25], which could be analyzed using EUV scatterometry. With the advent of lab EUV sources, this method could emerge as a real alternative to scanning methods [26,27] for the in-line metrology. EUV scatterometry has been already tested for the characterization of nanostructures [28–30]. However, it has not yet been rigorously benchmarked with more established and comparable scattering methods, such as GISAXS, and with a full description of uncertainty budgets.

We report, on the dimensional reconstruction of a lamellar grating using EUV scattering and its comparison to a GISAXS reconstruction. A dimensional reconstruction of a lamellar grating previously done using GISAXS [18] is here revisited, accounting for overseen sources of uncertainties [20]. The estimation of the parameter uncertainties is done by a Markov-Chain-Monte-Carlo (MCMC) method [31]. The results from GISAXS and EUV scatterometry are generally in good agreement. Additionally, we find that EUV scattering has several advantages over GISAXS. EUV allows to reduce the footprint on the targets. Also, it is shown that the computation times are reduced. Finally, EUV allows the identification and characterisation of oxide or contamination layers without the need for extra measurements.

2. Experimental details

The experiments were conducted at the PTB's soft X-ray beamline (SX700) [32] and the four-crystal monochromator (FCM) beamline [33] at the electron storage ring BESSY II. The SX700 beamline covers the energy range from 50 eV to 1800 eV and it is completely under UHV. The FCM covers a photon energy range from 1.75 keV to 10 keV.

The SX700 beamline is designed for a beam with small divergence and minimal halo. For the investigations, the EUV angle resolved scatter set-up [34] is used to measure across a wide solid angle of the scattered light by placing the CCD sensor close to the sample. This experimental set-up is illustrated in Fig. 1. A monochromatic EUV beam with a wavevector $\vec{k}_i$ impinges on the sample surface at a grazing incidence angle α_i. The elastically scattered wavevector $\vec{k}_f$ propagates with an exit angle α_f and an azimuth angle θ_f. And the scattering vector is $\vec{q} = \vec{k}_f - \vec{k}_i$,

$$\begin{pmatrix} q_x \\ q_y \\ q_z \end{pmatrix} = k_0 \begin{pmatrix} \cos(\theta_f)\cos(\alpha_f) - \cos(\alpha_i) \\ \sin(\theta_f)\cos(\alpha_f) \\ \sin(\alpha_f) + \sin(\alpha_i) \end{pmatrix}. \tag{1}$$

The sample can be rotated around φ, with the grating lines parallel to the scattering plane for $\varphi = 0$. A back-illuminated CCD camera is used. It has a (2048 x 2048) pixel area with a pixel size of 13.5 μm. The detector is placed close to the sample, at about 40 mm, allowing exit

Optics EXPRESS

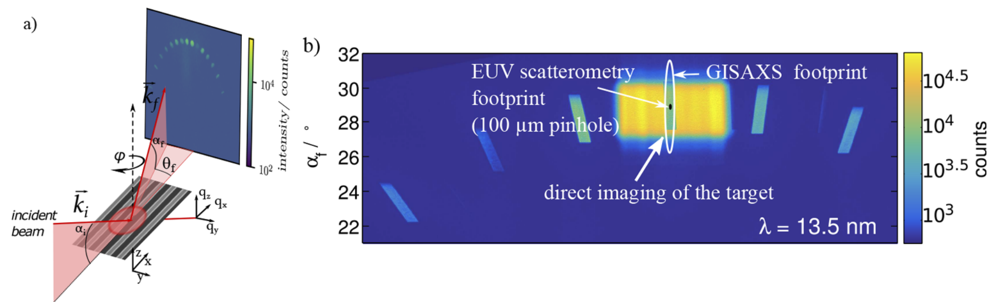

Fig. 1. **a)** Experimental set-up for EUV small angle scattering. **b)** CCD image of the grating diffraction rods obtained from a lamellar grating. The collimated incident beam allows a direct imaging of the sample area. Target areas can easily be identified by mapping the sample surface. The footprint between GISAXS and EUV is shown. By introducing a pinhole with a diameter of 100 μm in the beam path of the EUV scatterometry set-up, the probed area is reduced to 0.1 mm horizontally by 0.2 mm vertically.

angles of $\sim 30°$. This set-up has already been reported elsewhere [34]. By using a collimated beam large areas can be investigated (see Fig. 1(b)). This can be used for the detection of large inhomogenities on the samples [34] and to navigate the sample. The footprint can be reduced by using a set of pinholes. Here, a 100 μm pinhole was used, which allows the investigation of smaller targets. In order to increase the amount of information about the nanostructures, the reciprocal space was mapped. For this, the energy of the incoming photon beam was tuned from 210 eV to 230 eV in steps of 1 eV. The photon flux before the pinhole goes from $3.4{\cdot}10^9$ to $3.18{\cdot}10^9$ photons $\cdot$ s^{-1} at this energy range. After the pinhole around 4% of that flux is expected. The divergence of the beam was about $(0.09 \times 0.02)°$ in the horizontal and vertical direction, respectively. The acquisition time for each pattern was 100 s.

The conical mounting was also used in the FCM beamline, where the acquisition of GISAXS was done. This measurement has already been described elsewhere [20]. A beam-defining pinhole of about 500 μm was used at a distance of about 1.5 m to the sample. Together with a scatter guard of 1000 μm close to the sample, the beam spot size was about 0.5 mm *x* 0.5 mm at the sample position. The beam had a horizontal divergence of 0.01° and a vertical divergence of 0.006 °. The in-vacuum PILATUS 1M detector [35], with a pixel size of (172 x 172) μm^2, was placed at about 3.5 m. The incidence angle is $\alpha_i = 0.85°$. In order to obtain more information on the structures, several parts of the reciprocal space were mapped by varying the photon energy. Three photon energies were used for this study: 6 keV, 6.05 keV, and 6.1 keV. The photon flux at this energies is about $5.9{\cdot}\ 10^9$ photons s^{-1}. The acquisition time for each pattern was 2 s. The set-up looks similar to the one show in Fig. 1(a) but with smaller incidence angle α_i, which leads to the elongation of the footprint.

Figure 1(b) shows the footprint comparison between GISAXS and EUV. Compared to GISAXS, EUV scatterometry allows the heavy reduction of the footprint of the beam onto the targets. GISAXS does not allow the illumination using steeper angles if high surface sensitivity is pursued. Although, larger incident angles might used, usually they are not larger than five times the critical angle to probe the structured surface [36–38].

The sample consists of a state-of-the-art Si-lamellar grating produced by e-beam lithography. It has a pitch of 150 nm, a nominal height of 120 nm and a nominal line width of 65 nm. The structured area is 4 mm long in the direction of the grating lines and 0.5 mm wide. This structure was previously reconstructed using GISAXS without accounting for the vertical divergence of the beam, which is actually the leading error contribution [20]. The reconstruction using GISAXS is

revisited here using a more versatile method to account for the uncertainties and thereby, a more reliable confidence interval estimation.

3. Characterization of the line shape

The reconstruction of nanostructures from the diffracted intensities corresponds to an optimization problem based on the forward calculation of the experimental realization (including the model of the line). The computation of the forward model can be done by different methods [39]. Distorted-wave Born approximation has been broadly used for the characterization of the nanostructures [17,40–47]. Nevertheless, they are not as reliable as rigorous methods when the exact intensity distribution is pursued [22]. Rigorous methods, such as Maxwell solvers based on finite elements, have already been used for the characterization of periodic nanostructures [18,20,21]. The reconstruction of a nanostructure using EUV scatterometry has been previously tested [29]. However, no absolute scattered intensities were considered nor a thoughtful description of the experimental conditions. This prevents the derivation of realistic parameter uncertainties. The faithful reconstruction of a nanostructure relies on a good describing model of the experimental set-up. It has already been reported that the divergence of the light has a big impact on the diffracted intensities from GISAXS and thus, in the reconstruction of the nanostructures [18,20]. As well, the reconstruction of an error model in the optimization process allows the derivation of reliable error budgets [20].

The diffracted intensities are computed by a Maxwell solver based on the finite element method (FEM). Here, the commercial software *JCMsuite* is used [48]. It allows the rigorous computation of the near field distribution of any arbitrary shape. By a post-process based on a Fourier transformation the intensity of the diffraction orders is obtained. To sample the posterior distribution MCMC is used [31]. The posterior probability of the parameters depends on previous knowledge on the distribution of the parameters, which is the prior function, and on the likelihood function of the set of parameters.

The likelihood is given by,

$$\vec{L}(\sigma, \vec{e}) = \prod_{E,m} [2\pi\sigma^2(m, E)]^{-1/2} \exp(-\chi^2(\vec{e}, m, E)/2), \tag{2}$$

and $\chi^2(\vec{e}, m, E)$ corresponds to.

$$\chi^2(\vec{e}, m, E) = \frac{\left[I_{calc}\left(\vec{e}, m, E\right) - I_{exp}\left(m, E\right)\right]^2}{\sigma^2(m, E)}. \tag{3}$$

where m is order of diffraction, E is the energy and $\vec{e}$ are the variable parameters that are reconstructed. Usually the incoming incidence angle and the azimuthal rotation are included in the reconstruction together with the parameters defining the line shape. The bandwidth of the incident photon energy is also considered, with a Gaussian prior.

The calculated intensity I_{calc} includes a Debye-Waller factor to account for the effect of the roughness on the diffraction orders [20,49], $I_{calc} = I_{FEM} \exp(-q_y^2 \xi^2)$. And I_{FEM} is the computed intensity using the Maxwell solver. The standard deviation $\sigma(m, E)$ is composed by the experimental and computational errors. It has been reported that the reliable derivation of confidence intervals rely on a good determination of the uncertainties contributing to the methods. In order to account for possible unknown contribution, an error model must be used [20]. For virtual scattering experiments, an Gaussian error model has been identified by Heidenreich et al. [50]. The cases of EUV and GISAXS are discussed separately.

3.1. GISAXS

The description of the divergence of the light is indispensable to obtain an unequivocal solution in the reconstruction of nanostructures using GISAXS [20]. Including the divergence in

the computation increases the computation times by more than twenty times compared to a computation where the divergence can be disregarded. Different angles must be computed separately and convoluted with the profile of the beam for each model computation. Even including the divergence in the reconstruction, approximations must be done. These approximations are leading the contribution to the total uncertainty of the method [20,51]. The impact of the divergence on the intensity for a comparable GISAXS experiment has been reported elsewhere [20]. Depending on whether the orders lie on the reciprocal space (q_z, q_y, q_x), the impact of the divergence is also different. So that, when different energies are considered, an error must be fitted for each of them,

$$\sigma^2(m,E) \approx \sigma^2_{\text{model}}(m,E) + \sigma^2_{\text{exp}}(m,E) = [a(E)I(m,E)]^2 + b^2(E) + \sigma^2_N(m,E) + \sigma^2_{hom}(E) \quad (4)$$

The experimental error is given by two known errors. One is the detector inhomogenity (σ_{hom}) [35], which is about 2%. Additionally, an uncertainty following the Poisson statistical distribution is considered $\sigma_N(m,E)$, where m is the order of diffraction, and E is the energy.

The factor b can be usually considered negligible and be omitted from the reconstruction [20,21]. However, here it was reconstructed to allow the identification of overseen contributions. The reconstruction was done by using three different photon energies. No more energies were added to not further increase the computation time. Due to the large footprint, larger than the target, the scattered intensities can not be normalized to the incoming intensity. Therefore a scale must be included in the reconstruction.

3.2. EUV scatterometry

For GISAXS the effect of the divergence is leading the uncertainty contribution but also the computation time. Thereby, the impact of the divergence on the diffracted intensities was studied previous its inclusion in the computation. Figure 2(a) show the divergence of the light for this experiment in the EUV and with an incident angle of $\sim 30^\circ$. The divergence effect can be left out of the reconstruction process, which leads to a reduction in the computational time of each structure and experimental set-up. The error model in this case is,

$$\sigma^2(m,E) \approx \sigma^2_{\text{model}}(m,E) + \sigma^2_N(m,E) = [a \cdot I(m,E)]^2 + b^2 + \sigma^2_N(m,E) \quad (5)$$

This reduces the number of the parameters considerably when including more energies in the reconstruction. The reconstructed Gaussian error model includes the contribution of the divergence, as exposed before, but also of the numerical precision. This latter error is due to the assumption that must be made in the computation in order to have a solution in reasonable times. Although differences in this error are expected [51] when varying the energy, the mapped range is only of 20 eV. And therefore, just one error might be sufficient.

The CCD was calibrated for the extraction of absolute intensities, see inset Fig. 2(b). Although the direct beam cannot be measured directly with the CCD, the incoming intensity was measured before entering the chamber (before the pinhole). The measured signal at the detector during the experiments is proportional to the photon flux. Therefore, one scale factor for all the energies must be also reconstructed. Figure 2(b) shows the conversion rate from counts at the detector to incoming photons. The extracted diffraction efficiencies are shown in Fig. 2(c).

The reconstructed line model was also varied. The lamellar grating was produced by plasma etching, which usually produces an oxide layer on the top of the structure. Due to the generally poor optical contrast between Si and SiO_2 in the X-ray region, GISAXS is not sensitive to this small oxide layer on the top of the structure. Measurements at the Si edge increase the contrast between Si and SiO_2 but they also would add more uncertainties to the method. Optical constants at an absorption edge are not that well-known as those far from the edges. Moreover, the uncertainty of the PILATUS detector also increases in this region [35]. However, EUV

Optics EXPRESS

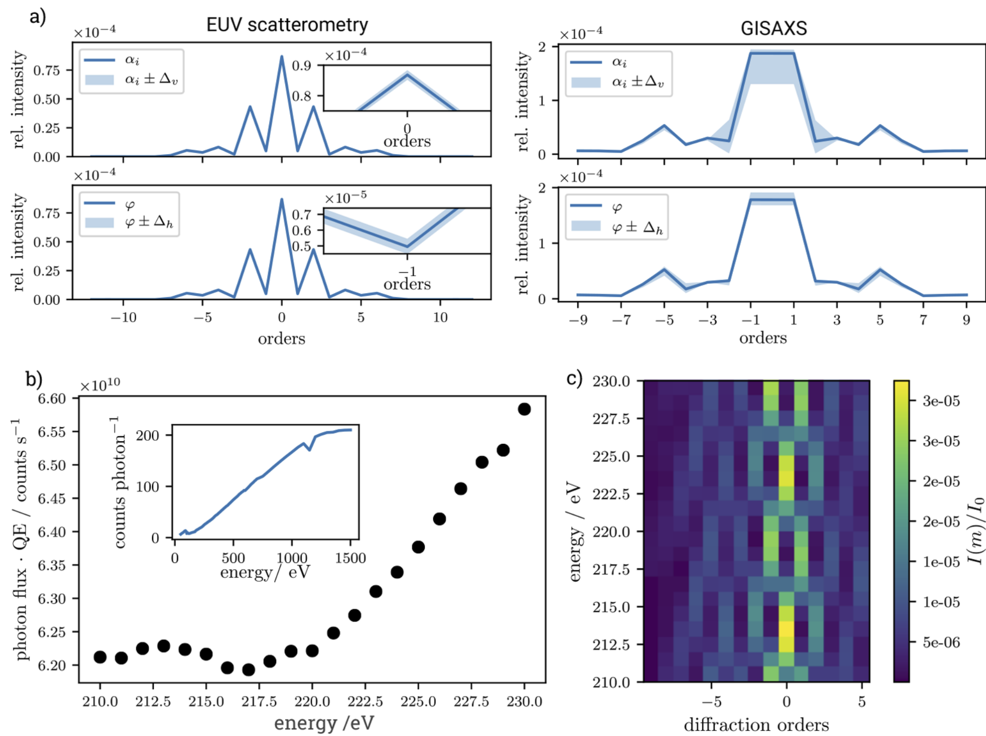

Fig. 2. **a)** Effect of the divergence in the intensity of the diffraction orders for EUV and GISAXS. The effect for GISAXS has been already published [20]. **b)** Conversion of the number of counts per photon per second. The inset shows the quantum efficiency of the CCD (counts per photon) for the whole energy range of the beamline. **c)** Diffraction efficiency of the diffraction orders as a function of the incident photon energy.

scatterometry might allow its characterization and thus, it must be considered in the reconstruction. Because oxide silicon usually has lower densities than bulk SiO_2, a weighting factor to the density of the oxide layer is also reconstructed. However, the optical constants are not reconstructed and tabulated data is used and scaled with the density.

4. Confidence intervals

The reconstruction was done by MCMC, using the emcee python package [31]. The analysis of the posterior distribution allows the investigation of the confidence intervals of the parameters. The search space was the same for both methods, except for the incident angles (φ, α_i). The search space for each parameter can be seen in Table 1 (limits column). The posterior distributions of both methods have multiple modalities. Although more experimental data points (more energies) were included in the EUV reconstruction, an unequivocal solution in the whole searched space is not found. The relatively large search space for the reconstruction of the incidence angles can be responsible for this behaviour, see Fig. 3(b). In GISAXS the angles are usually also reconstructed because diffracted intensities are very sensitive to any variation on the set-up [18]. But the search space is restricted to $\pm 0.02°$ of the measured angle and does not lead to a multi-modal posterior. However, in the EUV set-up [34] it was not possible to sufficiently calibrate these angles and they were reconstructed allowing comparably large search spaces. Actually the relative unknown incident angles have a strong influence on the observed modalities. The multiple modalities are

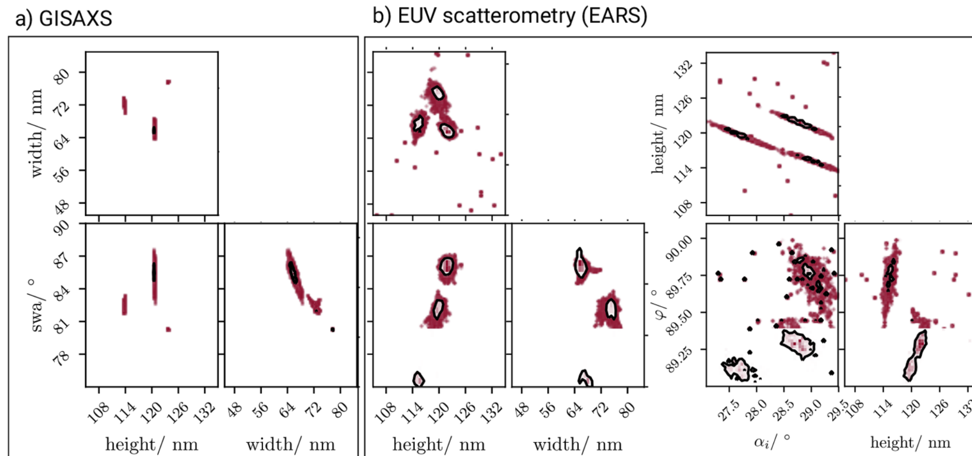

Fig. 3. Corner plots showing low-dimensional projections of the posterior distribution for GISAXS (**a**)) and EUV (**b**)). The black contours show 68% of the mass of the projected posterior distribution. The posteriors for EUV scatterometry (**b)** right) shows the dependency of the multiple modalities with the angle of incidence and azimuthal rotation.

observed with a certain correlation between the angles and the parameters. Here the width and height are shown.

Table 1. Values of the parameters defining the line profile obtained by the reconstruction done using MCMC from GISAXS data and EUV scatterometry. For GISAXS is shown the value and the confidence interval when considering 68% of the mass. For comparison (last two columns on the right), an area around the nominal height of the structure is chosen. The confidence intervals are obtained from the posterior distributions, considering 1σ. SiO_2 density corresponds to a weighting factor that is fitted to the density, which is considered to be the bulk density of 2.2 g/cm^{-3}.

	value ± confidence interval		value ± 1 σ (restricting l_h = [117,123])	
parameter	GISAXS	limits	GISAXS	EUV
height/ nm	$120.49^{+0.07}_{-0.12}$	[105,135]	120.49 ± 0.07	121.7 ± 0.8
height oxide / nm	-	-	-	3.89 ± 0.05
SiO_2 density	-	-	-	0.78 ± 0.02
line width/ nm	$65.7^{+1.4}_{-0.7}$	[45,85]	65.7 ± 0.7	65.8 ± 0.8
swa/ °	$85.31^{+0.8}_{-1.12}$	[75,90]	85.41 ± 0.7	86.0 ± 0.5
top rounding/ nm	$10.3^{+1.4}_{-0.9}$	[1,20]	10.15 ± 0.8	17.1 ± 1.1
bottom etch/nm	$11.1^{+0.9}_{-0.9}$	[1,15]	11.2 ± 0.7	11.7 ± 0.3
ξ/ nm	$0.98^{+0.3}_{-0.3}$	[0,7]	1.0 ± 0.3	3.22 ± 0.13
a[a] / %	15 ± 3	[0,30]	14 ± 3	15 ±3
b[b] / counts	-	-	-	857 ± 97

[a]the reconstructed error for GISAXS is given at 6 keV, plus the uncertainty of the detector. So that the total error of the method can be compared. In EUV this possible error was also reconstructed
[b]the obtained value for GISAXS correspond to less than one count per pixel

For GISAXS the posterior distributions were also analysed. A slight cross-correlation is observed for the line width and sidewall angle, see Fig. 3(a). The line width is defined at the middle of the height, which can be responsible for this observed behaviour for a certain measurement set-up. Depending on the measurement geometry, the sensitivity of the parameters

Optics EXPRESS

to the method might also change. Nevertheless, if the method were insensitive to one parameter, there would not be a defined solution of the posterior, which is here not the case.

The confidence intervals defined at 68% of the mass are given on Table 1. Usually the observed multi-modalities lead to a non-gaussian distribution of the confidence intervals depending on the selected limits of the search space, see second column on Table 1. For a better comparison between the two characterization methods, an area from the search space is selected around the nominal values of the structural parameters. In this case, just one solution is found and 1σ uncertainties can be estimated (see third column on Table 1).

5. Comparison between EUV scatterometry and GISAXS

The main consequence of the different wavelengths of the set-up is the different angles of incidence which are needed for surface sensitive analysis. Thereby, the projection of the footprint into the sample is very different. In GISAXS, the grazing angle of incidence is very small to probe the structured surface, $\alpha_i = 0.85\circ$, and the investigated surface is about (0.5×33) mm. On the other hand, EUV uses a much larger angle of incidence, α_i= 28.7$\circ$, and a pinhole was introduced in the beam path, so that the illuminated area is about (0.1×0.21) mm. The further reduction of the footprint in GISAXS using a pinhole is feasible. However, due to the shallow angles of incidence the elongation of the footprint is generally around 100 times larger than the beam size. Increasing the angle would lead to a decrease on the sensitivity to the surface and its imperfections.

It was reported that the forward model for the characterization of nanostructures using scattering data must consider the divergence of the beam [20]. Here, the same forward model was used. However, a preliminary analysis of the impact of the divergence on the diffracted intensities shows that larger incident angles, as in EUV, impact less the diffracted intensities. It would be advisable to use sources with reduced divergence for GISAXS applications. Nevertheless, the momentum transfer in q_y is similar in EUV and GISAXS but the large angle of incidence allows higher resolution in EUV despite of comparable beam divergence. In particular, in GISAXS the diffraction orders close to the horizon might appear or disappear with small variations of the incident angles, which strongly affects the intensity of the remaining diffraction orders. Despite longer measurement times in EUV scatterometry, not taking divergence into account in the reconstruction greatly reduces the computation time. This reduces the total reconstruction time, which is more time consuming than the measurement.

Figure 4 shows the comparison between the best fit and the measured data for each case: GISAXS (a)) and EUV (b)). The structure is reconstructed using analogous methods for EUV and GISAXS. The reconstruction of the line-shape relies on an optimization problem based on the computation of a forward model, which considers aspects as the beamline divergence. The layout for the EUV reconstruction was changed to allow the characterization of an oxide layer on the top of the structure. The comparison between both layouts is shown in Fig. 4(c). There is a slight difference on the line shape between the reconstruction using GISAXS and EUV scatterometry but they are in overall good agreement.

For the comparison of both methods the search space is constrained around the nominal value of the height, that is $height \in [117, 123]$. The comparison of the values is given in Table 1. Both methods are in good agreement and deliver analogous result for the geometry of the structure. The reconstructed amplitude of the roughness is not within the uncertainty. The reconstruction was done using a Debye-Waller factor.

The samples were measured with a time lapse of a few years, which could have cause the addition of a small contamination layer that is here not considered and that could have damped more the intensity of the diffraction orders.

Another explanation is the main difference between the two methods: each of them in an energy range and with different angle of incidence and thus, a very different footprint. Although

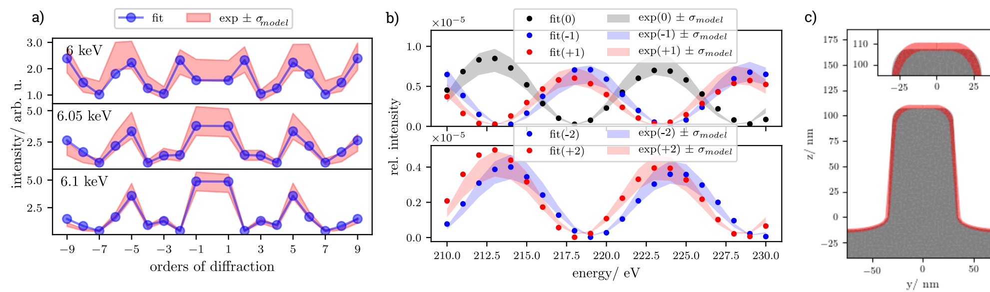

Fig. 4. **a), b)** Comparison between the measurement data and the best fit. The shaded area indicates the total error of the method using GISAXS (**a**)) and using EUV scattering (**b**)). For demonstration proposes, the total error (reconstructed and experimental errors) was applied to the experimental data. In this latter case, just the modulation of a few diffraction orders is shown (the diffraction order is given in parentheses). **c)** The gray area corresponds to the reconstructed line shape using GISAXS, on the top, a SiO_2 layer (semi-transparent red) corresponds to the line profile and oxide layer reconstructed using EUV scatterometry. A slightly difference on the line height and on the corner rounding is observed.

EUV still delivers ensemble results, the measurement is more local than GISAXS. It is also worth thinking whether the reconstructed roughness with each method corresponds to the same roughness. Although we have comparable q_y ranges in the experiment, the q_x component is completely different. Nevertheless, in the EUV energy range possible errors of the optical constants when assuming tabulated data cannot be completely ruled out.

The reconstructed error contributing to each method is also comparable between GISAXS and EUV. In EUV the zeroth order of diffraction was included in the reconstruction while in GISAXS, it is not due to the elongated footprint. Therefore, the illumination of surrounded areas is not an issue for the total uncertainty of the method if there are still enough diffraction orders that can be considered for the reconstruction and are not affected by other signals. In GISAXS no offset b of the error is observed, which can be explained by the hybrid photon-counting detector. Nevertheless, the uncertainty on the angles of the incoming beam in EUV must be addressed, to avoid the multiple modalities of the solution.

The combination of both methods might be an option when different q_x ranges are investigated. For instance, for different periodicities along the lines [20,52]. However, the registered q_y values are comparable and from these results it is inferred that the line-shape information is analogous in both methods. The combination of scattering with other signals, such as fluorescence can be of interest as this is adding extra information about the structure. This multi-method approach has already been tested for multilayer systems [53] and the analysis of grazing-incidence X-ray fluorescence data (GIXRF) has shown high sensitivity to the spatial distribution of the elements in periodic nanostructures [54].

6. Conclusions

The reconstruction of a lamellar grating was done using GISAXS and EUV scatterometry. In comparison to GISAXS, EUV allows the investigation of smaller areas, which is of high interest for the investigation of small targets. The same reconstruction procedure has been applied to each of the data sets. Due to the high sensitivity of GISAXS to the photon beam divergence, this must be included in the reconstruction. However, for EUV this is not anymore an issue, which saves computation time for each set-up. Moreover, the high optical contrast in EUV photon energy allows the identification of small oxide layers on the top of the structures. Both methods show an overall agreement between the reconstructed parameter values. Only the roughness

amplitude which was fitted by including a Debye-Waller factor in the reconstruction delivers different values. This is subject to further investigations and might be due to a contamination layer that has grown over time or to different sensitivity to the roughness contributions of the respective methods. The smaller footprint and higher experimental robustness with regard to parameters such as photon beam divergence make EUV scattering a promising method for the characterization of nanostructures.

Funding. Electronic Components and Systems for European Leadership (826589).

Acknowledgments. The authors would like to acknowledge the funding from the Electronic Component Systems for European Leadership Joint Undertaking under grant agreement No 826589—MADEin4. This Joint Undertaking receives support from the European Union's Horizon 2020 research and innovation programme and Netherlands, France, Belgium, Germany, Czech Republic, Austria, Hungary and Israel.

Disclosures. The authors declare no conflicts of interest.

Data availability. Data underlying the results presented in this paper are not publicly available at this time but may be obtained from the authors upon reasonable request.

References

1. N. G. Orji, M. Badaroglu, B. M. Barnes, C. Beitia, B. D. Bunday, U. Celano, R. J. Kline, M. Neisser, Y. Obeng, and A. E. Vladar, "Metrology for the next generation of semiconductor devices," Nat. Electron. **1**(10), 532–547 (2018).
2. B. Bunday, "HVM metrology challenges towards the 5nm node," in *Metrology, Inspection, and Process Control for Microlithography XXX*, vol. 9778 M. I. Sanchez, ed., International Society for Optics and Photonics (SPIE, 2016), pp. 136–169.
3. R. Kris, O. Adan, A. Tam, A. Y. Karabekov, O. Menadeva, R. Peltinov, A. Pnueli, O. Zoran, and A. Vilenkin, "Height and sidewall angle SEM metrology accuracy," in *Metrology, Inspection, and Process Control for Microlithography XVIII*, vol. 5375 R. M. Silver, ed., International Society for Optics and Photonics (SPIE, 2004), pp. 1212–1223.
4. J. Villarrubia, A. Vladár, B. Ming, R. Kline, D. Sunday, J. Chawla, and S. List, "Scanning electron microscope measurement of width and shape of 10 nm patterned lines using a JMONSEL-modeled library," Ultramicroscopy **154**, 15–28 (2015).
5. G. Dai, L. Xu, and K. Hahm, "Accurate tip characterization in critical dimension atomic force microscopy," Meas. Sci. Technol. **31**(7), 074011 (2020).
6. G. Dai, K. Hahm, F. Scholze, M.-A. Henn, H. Gross, J. Fluegge, and H. Bosse, "Measurements of cd and sidewall profile of euv photomask structures using cd-afm and tilting-afm," Meas. Sci. Technol. **25**(4), 044002 (2014).
7. M. Calaon, M. H. Madsen, and R. Leach, "Scatterometry," in *CIRP Encyclopedia of Production Engineering*, T. I. A. for Production, ed. (Springer Berlin Heidelberg, Berlin, Heidelberg, 2018), pp. 1–5.
8. D. F. Sunday and R. J. Kline, "X-Ray Metrology for Semiconductor Fabrication," in *Metrology and Diagnostic Techniques for Nanoelectronics*, Z. Ma and D. G. Seiler, eds. (Pan Stanford, Singapore, 2017), pp. 31–64.
9. T. Hu, R. L. Jones, W.-l. Wu, E. K. Lin, Q. Lin, D. Keane, S. Weigand, and J. Quintana, "Small angle x-ray scattering metrology for sidewall angle and cross section of nanometer scale line gratings," J. Appl. Phys. **96**(4), 1983–1987 (2004).
10. C. Wang, R. L. Jones, E. K. Lin, W.-L. Wu, and J. Leu, "Small angle x-ray scattering measurements of lithographic patterns with sidewall roughness from vertical standing waves," Appl. Phys. Lett. **90**(19), 193122 (2007).
11. P. Lemaillet, T. A. Germer, R. J. Kline, D. F. Sunday, C. Wang, and W.-l. Wu, "Intercomparison between optical and x-ray scatterometry measurements of FinFET structures," Proc. SPIE **8681**, 86810Q (2013).
12. M. Tolan, W. Press, F. Brinkop, and J. P. Kotthaus, "X-ray diffraction from laterally structured surfaces: Total external reflection," Phys. Rev. B **51**(4), 2239–2251 (1995).
13. T. H. Metzger, K. Haj-Yahya, J. Peisl, M. Wendel, H. Lorenz, J. P. Kotthaus, and G. S. C. Iii, "Nanometer surface gratings on Si(100) characterized by x-ray scattering under grazing incidence and atomic force microscopy," J. Appl. Phys. **81**(3), 1212–1216 (1997).
14. M. Jergel, P. Mikulík, E. Majková, V. Luby, R. Sendeák, E. Pinčík, M. Brunel, P. Hudek, I. Kostic, and A. Konečníková, "Structural characterization of a lamellar W/Si multilayer grating," J. Appl. Phys. **85**(2), 1225–1227 (1999).
15. P. Mikulík, M. Jergel, T. Baumbach, E. Majková, E. Pincík, S. Luby, L. Ortega, R. Tucoulou, P. Hudek, and I. Kostic, "Coplanar and non-coplanar x-ray reflectivity characterization of lateral w/si multilayer gratings," J. Phys. D: Appl. Phys. **34**(10A), A188–A192 (2001).
16. M. Yan and A. Gibaud, "On the intersection of grating truncation rods with the Ewald sphere studied by grazing-incidence small-angle X-ray scattering," J. Appl. Crystallogr. **40**(6), 1050–1055 (2007).
17. H. S. Suh, X. Chen, P. A. Rincon-Delgadillo, Z. Jiang, J. Strzalka, J. Wang, W. Chen, R. Gronheid, J. J. d. Pablo, N. Ferrier, M. Doxastakis, and P. F. Nealey, "Characterization of the shape and line-edge roughness of polymer gratings with grazing incidence small-angle X-ray scattering and atomic force microscopy," J. Appl. Crystallogr. **49**(3), 823–834 (2016).

18. V. Soltwisch, A. Fernández Herrero, M. Pflüger, A. Haase, J. Probst, C. Laubis, M. Krumrey, and F. Scholze, "Reconstructing detailed line profiles of lamellar gratings from GISAXS patterns with a Maxwell solver," J. Appl. Crystallogr. **50**(5), 1524–1532 (2017).
19. M. Pflüger, V. Soltwisch, J. Probst, F. Scholze, and M. Krumrey, "Grazing-incidence small-angle X-ray scattering (GISAXS) on small periodic targets using large beams," IUCrJ **4**(4), 431–438 (2017).
20. A. Fernández Herrero, M. Pflüger, J. Probst, F. Scholze, and V. Soltwisch, "Applicability of the Debye-Waller damping factor for the determination of the line-edge roughness of lamellar gratings," Opt. Express **27**(22), 32490–32507 (2019).
21. M. Pflüger, R. J. Kline, A. Fernández Herrero, M. Hammerschmidt, V. Soltwisch, and M. Krumrey, "Extracting dimensional parameters of gratings produced with self-aligned multiple patterning using grazing-incidence small-angle x-ray scattering," J. Micro/Nanolithogr., MEMS, MOEMS **19**(1), 014001 (2020).
22. M. Pflüger, "Using grazing incidence small-angle x-ray scattering (gisaxs) for semiconductor nanometrology and defect quantification," Ph.D. thesis, Humboldt-Universität zu Berlin, Mathematisch-Naturwissenschaftliche Fakultät (2020).
23. A. Haase, V. Soltwisch, S. Braun, C. Laubis, and F. Scholze, "Interface morphology of mo/si multilayer systems with varying mo layer thickness studied by euv diffuse scattering," Opt. Express **25**(13), 15441–15455 (2017).
24. Y.-J. Fan, L. Yankulin, P. Thomas, C. Mbanaso, A. Antohe, R. Garg, Y. Wang, T. Murray, A. Wüest, F. Goodwin, S. Huh, A. Cordes, P. Naulleau, K. Goldberg, I. Mochi, E. Gullikson, and G. Denbeaux, "Carbon contamination topography analysis of EUV masks," in *Extreme Ultraviolet (EUV) Lithography*, vol. 7636 B. M. L. Fontaine, ed., International Society for Optics and Photonics (SPIE, 2010), pp. 149–156.
25. H. J. Levinson and T. A. Brunner, "Current challenges and opportunities for EUV lithography," in *International Conference on Extreme Ultraviolet Lithography 2018*, vol. 10809 K. G. Ronse, E. Hendrickx, P. P. Naulleau, P. A. Gargini, and T. Itani, eds., International Society for Optics and Photonics (SPIE, 2018), pp. 5–11.
26. N. Truong, R. Safaei, V. Cardin, S. Lewis, X. Zhong, F. Légaré, and M. Denecke, "Coherent tabletop euv ptychography of nanopatterns," Sci. Rep. **8**(1), 16693 (2018).
27. M. Tanksalvala, C. L. Porter, Y. Esashi, B. Wang, N. W. Jenkins, Z. Zhang, G. P. Miley, J. L. Knobloch, B. McBennett, N. Horiguchi, S. Yazdi, J. Zhou, M. N. Jacobs, C. S. Bevis, R. M. Karl, P. Johnsen, D. Ren, L. Waller, D. E. Adams, S. L. Cousin, C.-T. Liao, J. Miao, M. Gerrity, H. C. Kapteyn, and M. M. Murnane, "Nondestructive, high-resolution, chemically specific 3d nanostructure characterization using phase-sensitive euv imaging reflectometry," Sci. Adv. **7**(5), eabd9667 (2021).
28. H. Gross, A. Rathsfeld, F. Scholze, and M. Bär, "Profile reconstruction in extreme ultraviolet (euv) scatterometry: Modeling and uncertainty estimates," Meas. Sci. Technol. **20**(10), 105102 (2009).
29. V. Soltwisch, C. Laubis, A. F. Herrero, M. Pflüger, A. Haase, and F. Scholze, "Investigating surface structures by EUV scattering," in *Extreme Ultraviolet (EUV) Lithography VIII*, vol. 10143 E. M. Panning, ed., International Society for Optics and Photonics (SPIE, 2017), pp. 142–152.
30. L. Bahrenberg, S. Danylyuk, S. Glabisch, M. Ghafoori, S. Schröder, S. Brose, J. Stollenwerk, and P. Loosen, "Characterization of nanoscale gratings by spectroscopic reflectometry in the extreme ultraviolet with a stand-alone setup," Opt. Express **28**(14), 20489–20502 (2020).
31. D. Foreman-Mackey, D. W. Hogg, D. Lang, and J. Goodman, "emcee: The MCMC hammer," Publ. Astron. Soc. Pac. **125**(925), 306–312 (2013).
32. F. Scholze, B. Beckhoff, G. Brandt, R. Fliegauf, A. Gottwald, R. Klein, B. Meyer, U. D. Schwarz, R. Thornagel, J. Tuemmler, K. Vogel, J. Weser, and G. Ulm, "High-accuracy EUV metrology of PTB using synchrotron radiation," in *Metrology, Inspection, and Process Control for Microlithography XV*, vol. 4344 N. T. Sullivan, ed., International Society for Optics and Photonics (SPIE, 2001), pp. 402–413.
33. M. Krumrey and G. Ulm, "High-accuracy detector calibration at the PTB four-crystal monochromator beamline," Nucl. Instruments Methods Phys. Res. Sect. A: Accel. Spectrometers, Detect. Assoc. Equip. **467-468**, 1175–1178 (2001).
34. A. Fernández Herrero, H. Mentzel, V. Soltwisch, S. Jaroslawzew, C. Laubis, and F. Scholze, "EUV-angle resolved scatter (EUV-ARS): a new tool for the characterization of nanometre structures," in *Metrology, Inspection, and Process Control for Microlithography XXXII*, vol. 10585 V. A. Ukraintsev, ed., International Society for Optics and Photonics (SPIE, 2018), pp. 140–148.
35. J. Wernecke, C. Gollwitzer, P. Müller, and M. Krumrey, "Characterization of an in-vacuum PILATUS 1M detector," J. Synchrotron Radiat. **21**(3), 529–536 (2014).
36. S. V. Roth, T. Autenrieth, G. Grübel, C. Riekel, M. Burghammer, R. Hengstler, L. Schulz, and P. Müller-Buschbaum, "In situ observation of nanoparticle ordering at the air-water-substrate boundary in colloidal solutions using x-ray nanobeams," Appl. Phys. Lett. **91**(9), 091915 (2007).
37. G. Santoro and S. Yu, "Grazing incidence small angle x-ray scattering as a tool for in- situ time-resolved studies," in *X-ray Scattering*, A. E. Ares, ed. (IntechOpen, Rijeka, 2017), chap. 2.
38. X. Lu, K. G. Yager, D. Johnston, C. T. Black, and B. M. Ocko, "Grazing-incidence transmission X-ray scattering: surface scattering in the Born approximation," J. Appl. Crystallogr. **46**(1), 165–172 (2013).
39. E. Popov, Ed., *Gratings: Theory and Numeric Applications* (Institut Fresnel, CNRS, Université d'Aix-Marseille, 2014), 2 revisited ed.

40. D. Babonneau, "*FitGISAXS*: software package for modelling and analysis of GISAXS data using IGOR Pro," J. Appl. Cryst. **43**(4), 929–936 (2010).
41. R. Lazzari, "*IsGISAXS*: a program for grazing-incidence small-angle X-ray scattering analysis of supported islands," J. Appl. Cryst. **35**(4), 406–421 (2002).
42. G. Renaud, R. Lazzari, and F. Leroy, "Probing surface and interface morphology with Grazing Incidence Small Angle X-Ray Scattering," Surf. Sci. Rep. **64**(8), 255–380 (2009).
43. D. R. Rueda, I. Martín-Fabiani, M. Soccio, N. Alayo, F. Pérez-Murano, E. Rebollar, M. C. García-Gutiérrez, M. Castillejo, and T. A. Ezquerra, "Grazing-incidence small-angle X-ray scattering of soft and hard nanofabricated gratings," J. Appl. Crystallogr. **45**(5), 1038–1045 (2012).
44. M. Rauscher, T. Salditt, and H. Spohn, "Small-angle x-ray scattering under grazing incidence: The cross section in the distorted-wave Born approximation," Phys. Rev. B **52**(23), 16855–16863 (1995).
45. Z. Jiang, D. R. Lee, S. Narayanan, J. Wang, and S. K. Sinha, "Waveguide-enhanced grazing-incidence small-angle x-ray scattering of buried nanostructures in thin films," Phys. Rev. B **84**(7), 075440 (2011).
46. T. Hofmann, E. Dobisz, and B. M. Ocko, "Grazing incident small angle x-ray scattering: A metrology to probe nanopatterned surfaces," J. Vac. Sci. Technol., B: Microelectron. Nanometer Struct.–Process., Meas., Phenom. **27**(6), 3238 (2009).
47. R. Meier, H.-Y. Chiang, M. A. Ruderer, S. Guo, V. Körstgens, J. Perlich, and P. Müller-Buschbaum, "In situ film characterization of thermally treated microstructured conducting polymer films," J. Polym. Sci. B Polym. Phys. **50**(9), 631–641 (2012).
48. S. Burger, L. Zschiedrich, J. Pomplun, and F. Schmidt, "JCMsuite: An Adaptive FEM Solver or Precise Simulations in Nano-Optics," in *Integrated Photonics and Nanophotonics Research and Applications*, (Optical Society of America, 2008), p. ITuE4.
49. A. Kato and F. Scholze, "Effect of line roughness on the diffraction intensities in angular resolved scatterometry," Appl. Opt. **49**(31), 6102–6110 (2010).
50. S. Heidenreich, H. Gross, and M. Bar, "Bayesian approach to the statistical inverse problem of scatterometry: Comparison of three surrogate models," Int. J. UncertaintyQuantification **5**(6), 511–526 (2015).
51. V. Soltwisch, A. Haase, J. Wernecke, J. Probst, M. Schoengen, S. Burger, M. Krumrey, and F. Scholze, "Correlated diffuse x-ray scattering from periodically nanostructured surfaces," Phys. Rev. B **94**(3), 035419 (2016).
52. A. Fernández Herrero, M. Pflüger, F. Scholze, and V. Soltwisch, "Fingerprinting the type of line edge roughness," in *Modeling Aspects in Optical Metrology VI*, vol. 10330 B. Bodermann, K. Frenner, and R. M. Silver, eds., International Society for Optics and Photonics (SPIE, 2017), pp. 175–183.
53. A. Haase, S. Bajt, P. Hönicke, V. Soltwisch, and F. Scholze, "Multiparameter characterization of subnanometre Cr/Sc multilayers based on complementary measurements," J. Appl. Crystallogr. **49**(6), 2161–2171 (2016).
54. V. Soltwisch, P. Hönicke, Y. Kayser, J. Eilbracht, J. Probst, F. Scholze, and B. Beckhoff, "Element sensitive reconstruction of nanostructured surfaces with finite elements and grazing incidence soft x-ray fluorescence," Nanoscale **10**(13), 6177–6185 (2018).